# Fractional PR Control of a Grid Tied Flying Capacitor Inverter for PV Applications

**Jaber Fallah-Ardashir[1,*], Amin Mohammadpour Shotorbani[2], Hossein Khoun-Jahan and Mehran sabahi[3]**

[1] Department of Electronics, Tabriz Branch, Islamic Azad University, Tabriz, Iran
[2] School of Engineering, University of British Columbia, Okanagan Campus, Kelowna, BC, Canada
[3] Faculty of Electrical and Computer Engineering University of Tabriz, Tabriz, Iran
*Corresponding author: j.fallah@iaut.ac.ir

**This paper presents a single-phase transformer-less Flying Capacitor Inverter (FCI) for grid-tied PV systems with Fractional Proportional Resonant (FPR) controller. In this structure, the neutral point of the grid is connected directly to the negative terminal of PV, so the Common Mode (CM) leakage current eliminate without using any control strategy. The main merits of this inverter are flexible grounding configuration and high safety. The FPR controller is employed for FCI. The low output current ripple of the FPR controller against parameter uncertainties is compared with conventional Proportional Resonant (PR) controller. The capability of controllers is investigated for parametric changes. The grid connected inverter can achieve the Maximum Power Point Tracking (MPPT) of the solar panels and inject a sinusoidal current into the grid with FPR controller. Finally, performance of the proposed controller scheme as well as the grid-tied FCI topology are verified through simulation results.**

## 1. Introduction

Recently, the Photovoltaic (PV) renewable energy systems have been widespread due to its numerous advantages, such as no carbon emissions and low requirements for maintenance [1]. As an integral clean source of energy in today's electrical power grid, high penetration of PV distributed generation requires further investigations in grid-connection of the PV systems [2]. In this regard, the high common mode current between the system ground and the solar PV panels is a critical operational problem, which degrades the efficiency of the PV power generating system and lowers its safety resulting in dangerous electric shocks [3]. Although galvanic isolation with power transformers can eliminate the PV system's leakage current, the adverse characteristics of the costly transformers [4] as heaviness, bulky size, and additional power loss restrict its applications. Therefore, transformer-less integration of PV systems to power grid reduces the costs and size, and improves the efficiency [5]. Galvanic isolation is a key challenge in transformer-less integration of distributed PV generation to power grid, due to presence of leakage current and the subsequent harms. Different inverter topologies have been proposed to minimize the leakage current [6, 7], including Full Bridge (FB) inverter, Neutral Point Clamped (NPC), active NPC [6], H5, H6, and HERIC inverters. The approach in these topologies is to disconnect the PV from the main grid while PV is the freewheeling operating mode [7]. With respect to switches' parasitic capacitance of the PV panel, the common mode or leakage current is not eliminated entirely [8]. Accordingly, filter inductors are utilized along with some topologies in order to

reduce the undesirable leakage current, resulting in a large volume and expensive costs [9]. Fig. 1 shows the block diagram of leakage current path in a grid-tied PV system through a transformer-less inverter. In this figure, $i_{Leakage}$ is the leakage current; $C_{PV1}$ and $C_{PV2}$ are the parasitic capacitors; $L_f$ and $L_g$ are inverter filter's and grid inductance, respectively.
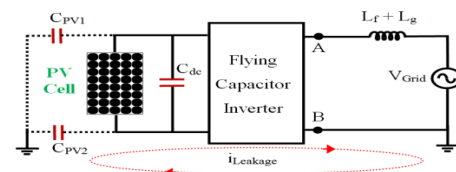


**Fig. 1.** Illustration of the path of common mode current in a grid-tied PV system

As shown in Fig. 1, the leakage current path consists of $C_{PV}$, $L_{f+}$ $L_g$, and the inverter. This current is hazardous and inefficient [10]. In Fig. 1, the common mode voltage (i.e. $v_{cm}$) is defined as:

$$v_{cm} = \frac{v_{An}L_2 + v_{Bn}L_1}{L_2 + L_1} \qquad (1)$$

where $v_{An}$ and $v_{Bn}$ are the voltage of points A and B with respect to N, respectively. The key approach to remove the common mode current, is to keep the Common Mode Voltage (CMV) at a constant value, for any operating mode [11].

## 2. Studied topology model

The three level NPC inverter as shown in Fig. 2 (a) has a similar structure as the traditional Half Bridge (HB) inverter with a connected midpoint of the dc link capacitors to the neutral point of the system ground. The NPC inverter has an improved efficiency and lower current ripple due to its three level output voltage. This inverter has low leakage current due to the low frequency components of the common mode voltage [12-14]. However, the input dc voltage requirement of the NPC inverter is twice of the grid peak voltage.

Topologies based on H6 are also proposed in [15] to eliminate the leakage current of the grid connected PV. As shown in Fig. 2 (b), these inverters consist of six power switches and two diodes for disconnecting the dc side from the utility grid during the zero-voltage level. For the positive and negative half cycle of the grid, the current flows through $S_4$, $D_1$ and $S_3$, $D_2$, respectively in the zero voltage state to disconnect the grid and PV module, therefore the leakage current is decreased. However, this topology is more costly than the FB inverter, because it uses extra switches and diodes. Another disadvantage of this topology is low efficiency because of the current circulates through three power switches in the positive and negative half cycle of the grid [16].
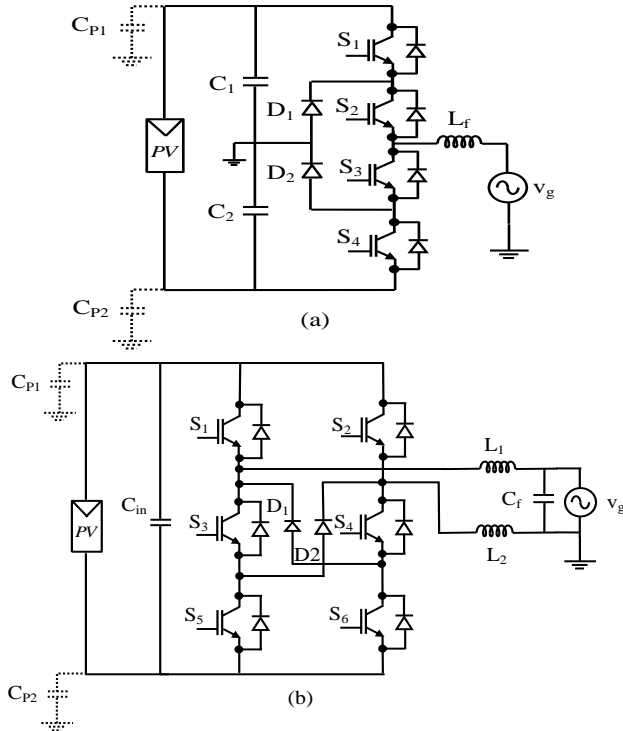


Fig. 2. Single phase grid connected transformer-less PV inverter topologies: (a) NPC inverter (b) H6 inverter

In [17], the charge pump circuit was used to propose a single-phase inverter for PV system as shown in Fig. 3. The charge pump circuit consist of two capacitors ($C_1$, $C_2$), two diodes ($D_1$, $D_2$), which is shown in Fig. 3. The negative output terminal of the inverter is directly connected to grid ground, to eliminate the leakage current, since parasitic capacitor's voltage is permanently set to zero. The negative voltage at inverter's output is generated through implementation of the charge pump circuit. Diverse modulation strategies can be used with topology[17], since the common mode current elimination is achieved through topology configuration.
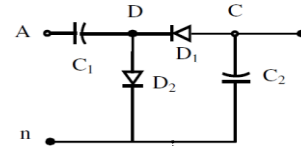


Fig. 3. Schematic diagram of the charge pump circuit [17]

The transformer-less inverter topology given in Fig. 4 consists of a charge pump circuit in addition to four power switches ($S_1$-$S_4$) [17]. The inverter is connected to the power grid through inductive filter. The SPWM modulation technique is used to drive the power switches and thus control the voltage of point A, based on the power switched.
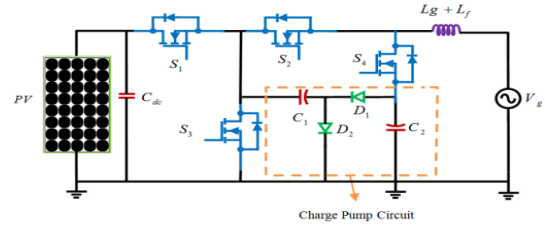


Fig. 4. A single phase transformer-less inverter for PV integration applications [17]

The operating region of this inverter is derived with respect to the current direction and voltage sign at point A, as illustrated in Fig. 5. As shown in Fig. 5(a), the switches $S_1$ and $S_2$ are on and the output voltage is $+V_{PV}$. When the switches $S_2$ and $S_3$ are on, the output voltage of Flying Capacitor Inverter (FCI) will be zero as shown in Fig. 5(b) and when the switches $S_1$ and $S_4$ are on, the output voltage of FCI will be negative voltage. The results of these operations are three level output voltage.



(a) ($v_{AN} = +V_{PV}$ , $i_g > 0$)



(b) ($v_{AN} = 0$ , $i_g > 0$)



(c) ($v_{AN} = -V_{PV}$ , $i_g > 0$)
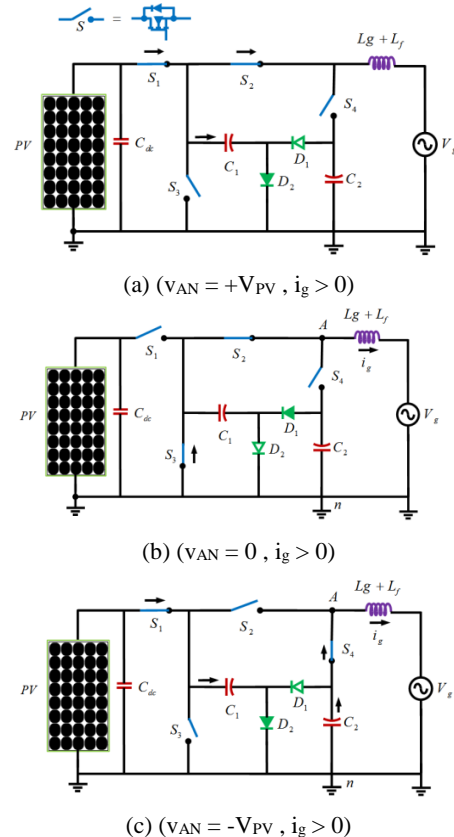
Fig. 5. The operating of transformerless FCI [17] (a) positive state (b) zero state (c) negative state
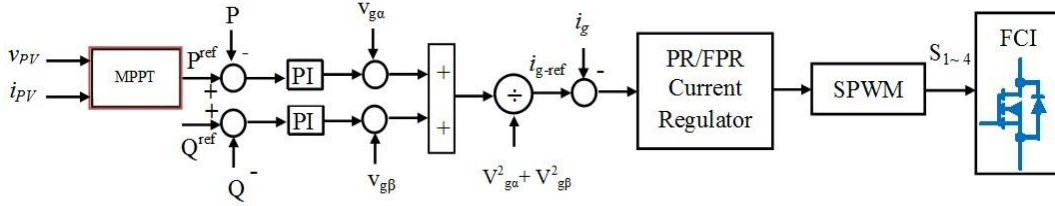
**Fig. 6.** Control block diagram of the proposed single phase grid tied inverter based on single phase PQ theory

## 3. Control scheme

Figure 6 depicts the control diagram for grid integration of the single-phase inverter in αβ stationary reference frame. There are two control loops [18] including the power controller as the outer loop and the current regulator as the inner loop.

The reference active power is determined from the MPPT block based on the voltage and current of the PV, to regulate the voltage of the capacitor CB. In Fig. 6, vgα and vgβ are the α-β components of the grid voltage in αβ stationary reference frame, respectively.

The power control loop provides the reference current for the inner loop, which has to generate a sinusoidal current for the SPWM block. Therefore, the power loop is a proportional-integral (PI) regulator, whereas the current regulator uses a proportional-resonant (PR) regulator [19]. The PR regulator is specific to track the sinusoidal current reference, though PI regulator is appropriate for dc reference values. PI and PR regulator are modeled in s-domain using the transfer functions (2) and (3), respectively.

$$G_{PI}(s) = K_P + K_I \frac{1}{s} \tag{2}$$

$$G_{PR}(s) = K_P + K_I \frac{\omega_n s}{s^2 + \omega_n^2} \tag{3}$$

where $K_p$ and $K_I$ are the real positive constants as the proportional and integral gains; $\omega_n = 2\pi f_n$ is the nominal resonant frequency, in which $f_n$ is the voltage nominal frequency.

The PR controller is corresponding to simultaneous combination of PI controller with two synchronous reference frames with contrary rotating directions. Two resonant complex poles are located at $s = \pm j\omega_n$ in a PR controller. For grid-integration applications based on reference frame transformation, it is suggested to include the gain $\omega_n$ in the numerator of PR transfer function [20].

The single-phase active and reactive powers are calculated as (4) and (5) respectively, based on the quadrature components of the output voltage and current [21].

$$P = \frac{1}{2}\left(v_{g\alpha} i_{g\alpha} + v_{g\beta} i_{g\beta}\right) \tag{4}$$

$$Q = \frac{1}{2}\left(v_{g\alpha} i_{g\alpha} - v_{g\beta} i_{g\beta}\right) \tag{5}$$

The current reference ($i_g^*$) is then calculated as (6), regarding the desired reference active and reactive powers (i.e. $P^*$ and $Q^*$) and the PI controllers [21].

$$i_g^* = \frac{1}{v_{g\alpha}^2 + v_{g\beta}^2}\begin{pmatrix} v_{g\alpha} & v_{g\beta} \end{pmatrix}\begin{pmatrix} G_{PI}^P(s) & 0 \\ 0 & G_{PI}^Q(s) \end{pmatrix}\begin{pmatrix} P - P^* \\ Q - Q^* \end{pmatrix} \tag{6}$$

where $G_{PI}^P(s)$ and $G_{PI}^Q(s)$ are the active and reactive power controllers defined in (6), respectively.

## 4. Fractional-order PR control

Fractional order calculus generalize the integer-order differentiation and integration to non-integer rational and irrational orders, in order to describe the systems and controllers with higher accuracy [22]. Various definitions have been proposed to describe the fractional-order integro-differential operator such as Riemann-Liouville (7) and Grünwald-Letnikov (8).

$$_aD_t^\gamma \xi(t) = \frac{1}{\Gamma(r-\gamma)} \frac{d^r}{dt^r} \int_a^t \frac{\xi(\tau)}{(t-\tau)^{\gamma-r+1}} d\tau \tag{7}$$

where $\Gamma(\cdot)$ is the Euler's Gamma function, a is the initial condition, and $r \in \mathbb{R}$ is an integer such that $r - 1 < \gamma < r$.

$$_aD_t^\gamma \xi(t) = \lim_{h \to 0} h^{-\gamma} \sum_{m=0}^{\left[\frac{t-a}{h}\right]} (-1)^m \binom{\gamma}{m} \xi(t-mh) \tag{8}$$

The operator $_aD_t^\gamma$ is described in s-domain by the notion (9) using the Laplace transform of the Riemann-Liouville definition (7) for a = 0 and $0 < \eta < 1$.

$$\mathcal{L}\left\{_0D_t^\eta f(t); s\right\} = F(s), 0 < \eta < 1 \tag{9}$$

where $F(s) = \mathcal{L}\{f(t); s\}$ is the Laplace transform of f(t).

Hybrid combination of the conventional PR controllers with the powerful fractional order calculus improves the control response of the current regulation scheme, in a wide range of frequency, by providing higher degree of freedom. The fractional-order PR controller is formulated as:

$$G_{PR}(s) = K_P + K_I \frac{s^\eta \omega_n}{s^2 + \omega_n^2}, 0 < \eta < 1 \tag{10}$$

However, practical application of non-integer fractional-order controllers in continuous time domain is the key challenge, due to extraordinary complexity of the fractional-order calculus. For

practical implementations, the calculated transfer function of the non-integer fractional-order in s-domain will not be a rational polynomial. Consequently, direct implementation of the fractional-order PI and PR controllers is not applicable. Therefore, different approximate implementations have been suggested by approximating the fractional-order terms, such as continued fraction expansion, Carlson's approximation, Matsuda's approximation, Oustaloup's approximation, and Chareff's approximation [23-25].

In this paper, the Oustaloup's approximation [25] of (11) is used for continuous-time formulation of $F(s) = s^{\eta}$ as:

$$F(s) \approx \sqrt{\omega_h \omega_l} \left( \frac{\omega_l}{\omega_h} \right)^{\frac{\eta}{2}} \prod_{k=1}^{2N+1} \frac{1 + \frac{s}{\omega_{zk}}}{1 + \frac{s}{\omega_{pk}}} \qquad (11)$$

where $\omega_l$ and $\omega_h$ are the lowest and highest frequency of the approximation band, respectively; $\omega_{zk}$ and $\omega_{pk}$ are the zeros and poles defined in (12) and (13), respectively; and $2N + 1$ is the entire number of zeros and poles.

$$\omega_{zk} = \omega_l \left( \frac{\omega_h}{\omega_l} \right)^{\frac{k - \frac{1}{2} - \frac{\eta}{2}}{2N+1}} \qquad (12)$$

$$\omega_{pk} = \omega_l \left( \frac{\omega_h}{\omega_l} \right)^{\frac{k - \frac{1}{2} + \frac{\eta}{2}}{2N+1}} \qquad (13)$$

In addition to the control gains (i.e. $K_P$ and $K_I$), the non-integer order $0 < \eta < 1$ can be tuned to attain the desired response. The order $\eta$ provides higher degree of freedom compared to conventional PR control with $\eta = 1$. The fundamental issue for a dynamic control loop to track a reference signal is to minimize the phase delay.

With identical control gains (i.e. $K_P$ and $K_I$) for fractional-order PR and the conventional PR controllers, the order $\eta$ could be in accordance with the desired delay value for high frequencies $\omega > \omega_n$ in (10). Although $\eta$ can be tuned with respect to the system gain magnitude at a specific frequency of $\omega > \omega_n$, tuning $\eta$ in terms of response phase is more effective for tracking problems.

## 5. Simulation results

### 5.1. THD comparison and effectiveness of different grid inductances

The flying capacitor transformer-less inverter with PR and FPR controllers is simulated in PSCAD/EMTDC. The system parameters and control parameters for the simulation results are presented in Table 1 and Table 2, respectively.

**Table 1.** Simulation Parameters

| Parameter | Value |
|---|---|
| Switching Frequency | 2kHz |
| Rated Power | 2Kw |
| Frequency | 50Hz |
| Grid voltage (RMS) | 220V |
| Parasitic capacitor | 10uF |
| $C_1$ and $C_2$ | 330uF |

**Table 2.** Control Parameters

| Parameter | Value |
|---|---|
| $w_l$ (rad/s) | 1 |
| $W_h$ (rad/s) | 60000 |
| N | 2 |
| $K_P$ | 1 |
| $K_I$ | 30 |

The test results of system are shown in Fig.7. The three level output voltage of FCI with grid injection current and leakage current are carried out in Fig. 7 (a), Fig. 7 (b) and Fig. 7 (c), respectively.

As shown in Fig.7 (c), the scale of leakage current waveform is very low and the magnitude of this current is approximately equal to zero and this shows the functionality of system for PV application. The magnitude of leakage current is in accordance with VDE standard and so the studied system has a high safety feature without any leakage current problem. The other important leakage current problem is the effectiveness of this current to grid injection current. The leakage current causes that the Total Harmonic Distortion (THD) current to be worsened. The PR and FPR methods are simulated to show the effectiveness of these controllers in single phase transformer-less grid tie FCI.
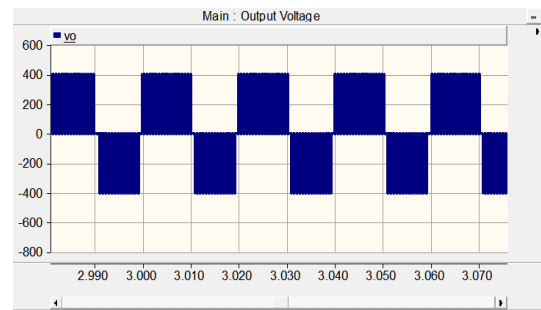


(a)
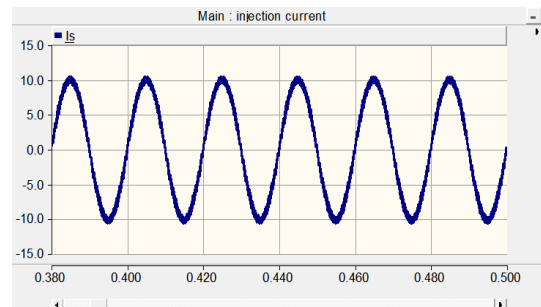


(b)
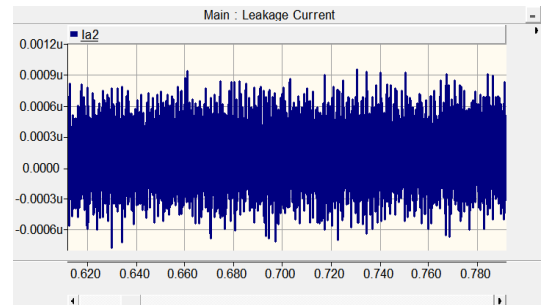


(c)

**Fig. 7.** (a) FCI output voltage, (b) grid injection current and (c) leakage current waveform.2.2. Data analysis

The simulated system with PR and FPR controllers are shown in Fig. 8 and Fig. 9, respectively. In the studied system, the magnitude of grid inductance has been changed in 3th second from 4mH to 2mH to show the effectiveness of various grid inductances on the quality of injection current. The THD graph for injection current with PR and FPR controllers are shown in Fig. 8 (a) and Fig. 9 (a), respectively. As shown in Fig. 8 (a), the THD value is almost 1.19% with 4mH inductance and this THD value is 4.08% with 2mH inductance. Also, the THD value for current injection with FPR controller is almost 0.42% with 4mH inductance and this THD value is 0.96% with 2mH inductance as shown in Fig. 9 (a). It is clear that the current THD has been changed with various grid inductances in 3th second in these figures. The simulated results show that the THD is lower for FPR controller than PR controller. The injection current waveforms with PR and FPR controllers are shown in Fig. 8 (b) and Fig. 9 (b). In these two controllers, when the grid inductor decreases suddenly, the quality of injection current is worsening.
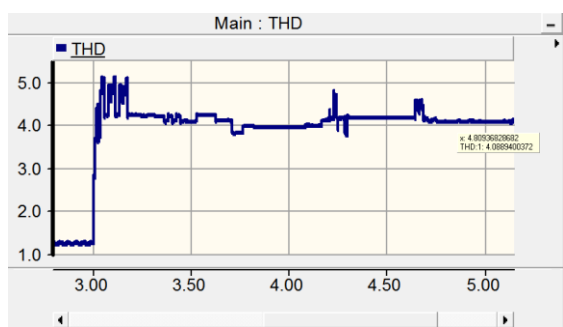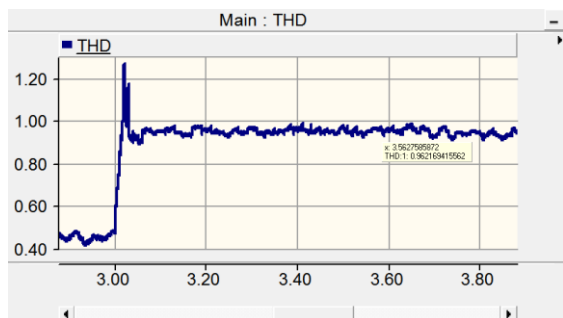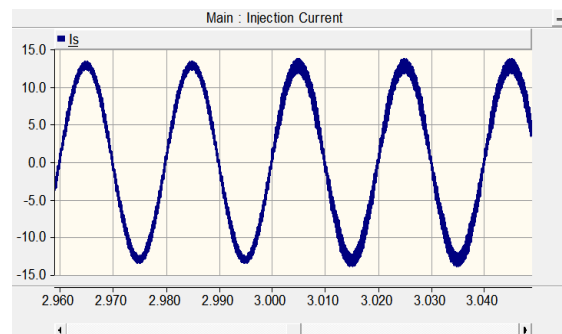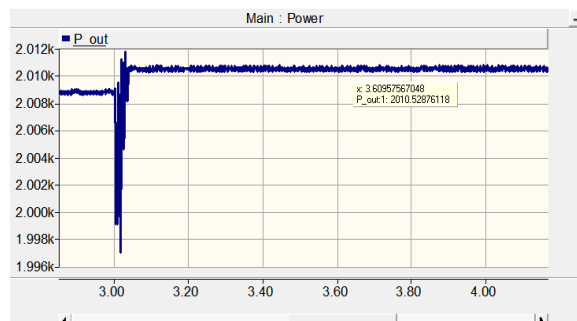


(a)
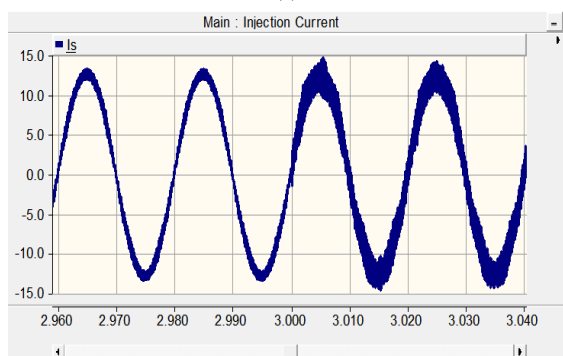


(b)

**Fig. 8.** (a) injection current THD, and (b) injection current waveform with PR controller
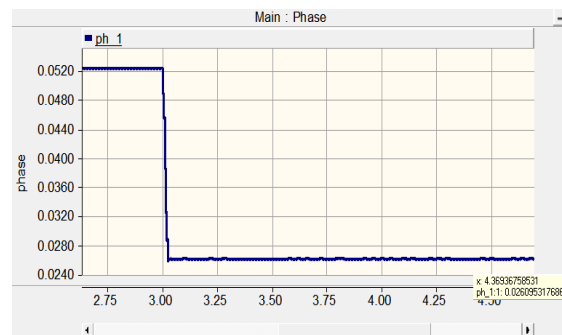


(a)



(b)



(c)



(d)

**Fig. 9.** (a) injection current THD, (b) injection current waveform, (c) output power, and (d) voltage phase of FCI with FPR controller

### 5.2. Maximum power point tracking of studied system

The system simulated with conventional dc/dc boost converter to show the capability of system for MPPT tracking. Fig.10 and Fig.11 are showing the simulation results of overall system with PV array, dc/dc conventional boost converter and FCI. Fig.10 shows the current and voltage simulated waveforms of PV in the grid connected mode. These parameters have low fluctuations that the average PV current is 7.2A and the average PV voltage is 293V. Fig.11 shows the P-V and I-V characteristics of PV according to simulation results. Fig. 11 (a) shows the maximum power point of PV is 2Kw and related voltage of this point is 283 V. This voltage has been increased to 400V with the conventional boost converter to prepare the proper voltage to the FCI. According to I-V characteristic of PV in Fig. 11 (b), the current and voltage of MPP are verified the Fig. 10 results.
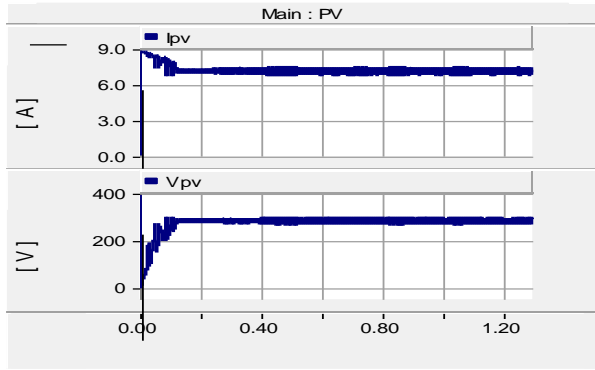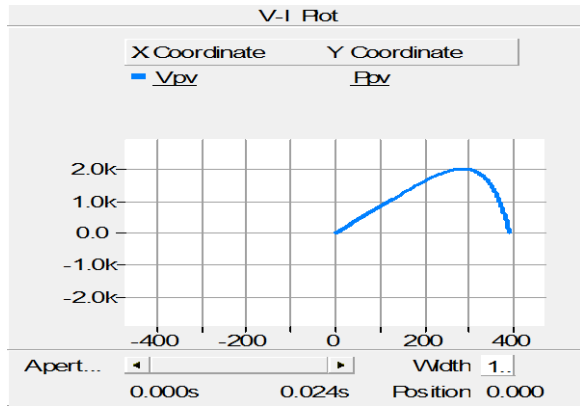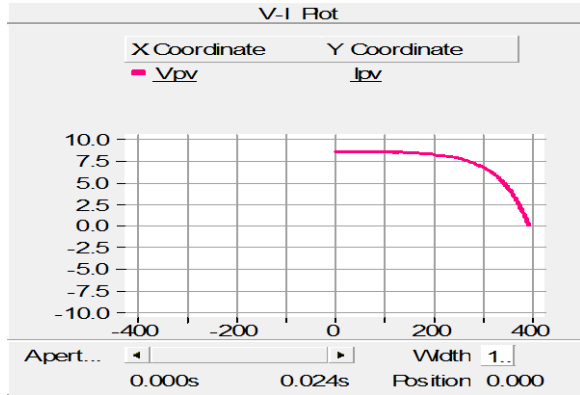
**Fig. 10.** The current and voltage simulated waveforms of PV



(a)



(b)

**Fig. 11.** (a) The P-V and (b) I-V curves of PV arrays in the grid connected system

### 5.3. Solar radiation profile changes

In this paper, the P&O method is used to track the maximum power point of PV system according to Fig.11. The sampling values of $i_{PV}$ and $v_{PV}$ have been given to MPPT block to produce maximum power point ($P_{max}$). The $P_{max}$ is the maximum power of PV and $V_{mpp}$ is the related voltage of MPP. The reference injection current is obtained using maximum power point of PV and the injection current to the grid has been controlled by PI controller. The active power reference (P*) can be tuned by the MPPT block diagram control system. The solar radiation profile changes from 2500w/m² to 2800w/m² in 4th second to validate the performance of system. Fig. 12 shows the variation of irradiation. As shown in Fig. 13, the maximum power related to PV is achieved with lowest oscillation in short duration. Fig. 13 validates the maximum power according to variations of weather condition in 4th second and the

maximum power of PV has been transfer with unit power factor to the grid. Fig. 14 shows the simulation system results with irradiation different in 4th second for injection current to grid ($i_s$), grid voltage ($v_g$) and inverter output three level voltage before filter ($v_{AN}$). As seen in these figures, the injection current of MPPT has low ripple.



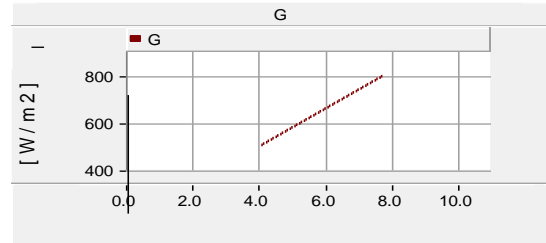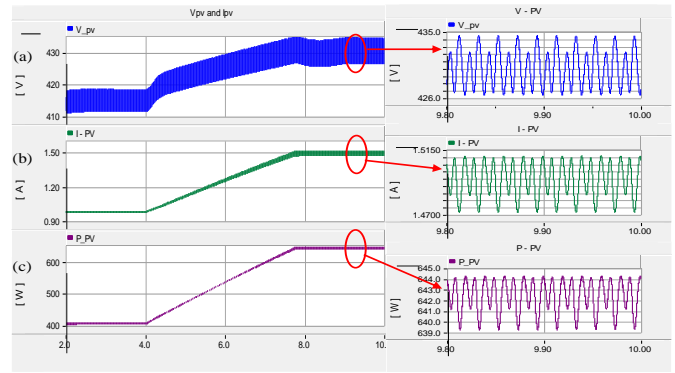**Fig. 12.** The irradiation changes of PV profile



**Fig. 13.** (a) The output voltage of PV ($v_{PV}$), (b) the output current of PV($i_{PV}$) and (c) the output power of PV ($P_{PV}$)
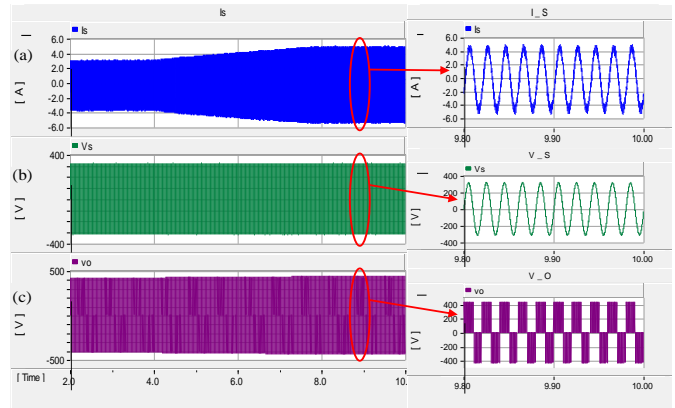


**Fig. 14.** (a) The injection current to grid ($i_s$), (b) the grid voltage ($v_s$) and (c) the output three level voltage ($v_o$)

### 6. Conclusion

A single stage flying capacitor grid-tie inverter is evaluated in this paper. This FCI removed the leakage current because the negative terminal of PV has the same point with natural of grid. The PR and FPR controllers employed for FCI. A comparison of injection current THD with FPR and PR methods compared with each other and showed that the FPR method is better than PR controller in this feature. This structure is connected to PV module to achieve MPPT. The conventional P&O algorithm is performed to achieve the maximum power point from PV module in different solar radiation conditions. The simulation output power results, grid voltage and current injection to the grid have been presented with various weather conditions. It is observed that the structure tracks the maximum power point quickly with environment changes.

## References

[1] Ji, B., J. Wang, and J. Zhao. "High-efficiency single-phase transformerless PV H6 inverter with hybrid modulation method." *IEEE Transactions on Industrial Electronics*, vol. 60, (2013): 2104-2115.

[2] Shao, Z., X. Zhang, F. Wang, R. Cao, and H. Ni. "Analysis and Control of Neutral-Point Voltage for Transformerless Three-Level PV Inverter in LVRT Operation." *IEEE Transactions on Power Electronics*, vol. 32, (2017): 2347-2359.

[3] Ardeshir, J. F., A. Ajami, A. Jalilvand, and A. M. Shotorbani. "Flexible Power Electronic Transformer for Power Flow Control Applications." *Journal of Operation and Automation in Power Engineering*, vol. 1, no. 2, (2013): 147–155.

[4] Woo-Jun, C., K. Kyu-Tae, C. Yong-Won, L. Sung-Ho, and K. Bong-Hwan. "Evaluation and analysis of transformerless photovoltaic inverter topology for efficiency improvement and reduction of leakage current." *IET Power Electronics*, vol. 8, no. 2, (2015): 255–267.

[5] Hu, H., W. Al-Hoor, N. Kutkut, I. Batarseh, and Z. J. Shen. "Efficiency improvement of grid-tied inverters at low input power using pulse skipping control strategy." *Twenty-Fifth Annual IEEE Applied Power Electronics Conference and Exposition (APEC)*, 2010: 627-633.

[6] Brückner, T., S. Bernet, and H. Güldner. "The active NPC converter and its loss-balancing control." *IEEE Trans. Ind. Electron.*, vol. 52, no. 3, (2005): 855-868.

[7] Barater, D., E. Lorenzani, C. Concari, G. Franceschini, and G. Buticchi. "Recent advances in single-phase transformerless photovoltaic inverters." *IET Renewable Power Generation,* vol. 10, no. 2, (2016): 260-273.

[8] Gu, Y., W. Li, Y. Zhao, B. Yang, C. Li, and X. He. "Transformerless inverter with virtual DC bus concept for cost-effective grid-connected PV power systems." *IEEE Transactions on Power Electronics,* vol. 28, (2013): 793-805.

[9] Yu, W., J. Lai, H. Qian, C. Hutchens, J. Zhang, G. Lisi, A. Djabbari, G. Smith, and T. Hegarty. "High-efficiency inverter with H6-type configuration for photovoltaic non-isolated ac module applications." *in Proc. IEEE APEC 2010*, (2010): 1056-1061.

[10] Yang, B., W. Li, Y. Gu, W. Cui, and X. He. "Improved transformerless inverter with common-mode leakage current elimination for a photovoltaic grid connected power system." *IEEE Trans. Power Electron.*, vol. 27, no. 2, (2012): 752 -762.

[11] Bradaschia, F., M. C. Cavalcanti, P. E. P. Ferraz, F. A. S. Neves, E. C. Santos, and J. H. G. M. Silva. "Modulation for three-phase transformerless z-source inverter to reduce leakage currents in photovoltaic systems." *IEEE Trans. Ind. Electron.*, vol. 58, no. 12, (2011): 5385–5395.

[12] Rodríguez, J., J. S. Lai, and F. Z. Peng. "Multilevel inverters: a survey of topologies, controls and applications." *IEEE Trans. Ind. Electron.*, vol. 49, no. 4, (2002): 724-738.

[13] Wanjekeche, T., A. A. Jimoh, and D. V. Nicolae. "A Novel 9-level multilevel inverter based on 3-level NPC/H-bridge topology for photovoltaic applications." *International Review of Electrical Engineering,* vol. 4, no. 5, (2009).

[14] Wang, Y. and R. Li. "Novel high-efficiency three-level stacked-neutral point-clamped grid-tied inverter." *IEEE Trans. Ind. Elect.*, vol. 60, no. 9, (2013): 3766-3774.

[15] Zhang, L., K. Sun, Y. Xing, and M. Xing. "H6 transformerless full-bridge PV grid-tied inverters." *IEEE Transactions on Power Electronics,* vol. 29, (2014): 1229-1238.

[16] Yu, W., J.-S Lai, H Qian, and C. Hutchens. "High-efficiency mosfet inverter with H6-type configuration for photovoltaic non isolated AC module applications." *IEEE Trans. on Power Electron.*, vol.26, no.4, (2011): 1253-1260.

[17] Ardashir, J. F., M. Sabahi, S. H. Hosseini, F. Blaabjerg, E. Babaei, and G. B. Gharehpetian. "A Single-Phase Transformerless Inverter with Charge Pump Circuit Concept for Grid-Tied PV Applications." *IEEE Trans. Ind. Electron.*, Vol.64, (2017): 5403-5415.

[18] Blaabjerg, F., R. Teodorescu, M. Liserre, and A.V. Timbus. "Overview of control and grid synchronization for distributed power generation systems."*IEEE Trans. Ind. Electron.*, vol. 53, no. 5, (2006): 1398–1409.

[19] Chen, W. L., and J. S. Lin. "One-dimensional optimization for proportional resonant controller design against the change in source impedance and solar irradiation in PV systems." *IEEE Trans. Ind. Electron.*, vol. 61, no. 4, (2014): 1845–1854.

[20] Rodrıguez, F. J., E. Bueno, M. Aredes, L. G. B. Rolim, F. A. S. Neves and M. C. Cavalcanti. "Discrete-time implementation of second order generalized integrators for grid converters." *IEEE Ind. Electron. Soc. (IECON)* no 1, (2008): 176- 181.

[21] Yang, Y., F. Blaabjerg, and H. Wang. "Low voltage ride-through of single-phase transformerless photovoltaic inverters." *IEEE Trans. Ind. Appl.*, vol. 50, no. 3, pp. 1942–1952, May/Jun. 2014.

[22] Podlubny, I.. "*Fractional Differential Equations.*"*San Diego, CA: Academic Press*, 1999.

[23] Charef, A., H. H. Sun, Y. Y. Tsao, and B. Onaral. "Fractal system as represented by singularity function." *IEEE Transactions on Automatic Control*, Vol 37 no 9, (1992): 1465- 1470.

[24] Shotorbani, A. M. and E. Babaei. "Robust Nonlinear Controller Based on Control Lyapunov Function and Terminal Sliding Mode for Buck Converter." *International Journal of Numerical Modelling,* vol. 29, (2016): 1055–1069.

[25] Oustaloup, A., F. Levron, F. Nanot, and B. Mathieu. "Frequency-band complex non-integer differentiator: characterization and synthesis." *IEEE Transactions on Circuits and Systems I: Fundamental Theory and Applications*, Vol. 47, (2000): 25–40.